Space Object Data Association Using Spatial Pattern Recognition Approaches

Aniketh Kalur*
University of Minnesota, Minneapolis, MN 55455

Steven A. Szklany† and John L. Crassidis‡
University at Buffalo, State University of New York, Amherst, NY 14260-4400

Closely-spaced objects, especially debris objects, create a setting that is very similar to a multi-target environment in a tracking problem. This environment engenders a major data association problem in the field of space situational awareness. To address this problem, an approach that couples gating methods for data association along with a star pattern recognition algorithm, called the planar triangular method, is developed. The planar triangular method has been shown to work effectively for spacecraft attitude determination using star trackers by comparing stars in field-of-view to those present in the catalog. This approach is further enhanced here for association of resident space objects. The planar triangle approach is further enhanced to associate closely spaced objects by incorporating a classical validation gate-based algorithm. The work in this paper shows the effectiveness of combining traditional data association methods with an existing planar triangle pattern recognition algorithm for space object association. Results indicate that the traditional gating algorithm significantly improves the planar triangular method's accuracy for space object association of closely-spaced clutters in highly uncertain environments.

I. Introduction

Space Situational Awareness (SSA) deals with collecting and maintaining knowledge of all objects orbiting the Earth. It is defined as the comprehensive knowledge of space objects and the ability to track, understand and predict their future location. The orbits in space are comprised of functional and defunct objects, as well as artificial objects. Functional objects are actively controlled so that their attitude and position can be maintained to accomplish mission objectives. However, defunct objects generally are not actively controlled for attitude and positional corrections. Inability to control objects in space renders them as "space junk;" these objects are rarely of any use and cause a threat to functional objects that are currently in orbit. Defunct objects are often spent rocket stages, inoperable satellites or parts of spacecraft that were once functional. Most uncontrolled objects are often referred to as orbital debris. Generally these objects do not follow pure Keplerian motion, being subjected to drift and decay. For example, variations in the Earth's gravitational field cause drift, which can lead to gradual movement of an object from one orbital plane to another. Atmospheric drag is a major cause of orbital decay, thereby causing a slow decrease in altitude of the object. Solar radiation pressure can also affect an object's orbit. Taken together, uncontrolled objects pose a difficult problem in maintaining adequate SSA.

A very common term associated with Resident Space Objects (RSOs) in space is *Kessler's syndrome*, which theorizes that creation of new debris occurs faster than the time taken by natural forces to remove them. As space object density increases, the collision between objects could cause a cascading effect, i.e. each collision generates more debris and thereby increases the likelihood of further collisions. There are more than

*Graduate Student, Department of Aerospace Engineering & Mechanics. Email: kalur002@umn.edu.
†Graduate Student, Department of Mechanical & Aerospace Engineering. Email: sszklany@buffalo.edu.
‡CUBRC Professor in Space Situational Awareness, Department of Mechanical & Aerospace Engineering. Email: johnc@buffalo.edu. Fellow AIAA.

21,000 piece of debris with a radius larger than 10 centimeters. These 21,000 pieces of debris are open to the same threat of collisions as defined by the Kessler's syndrome. A recent consequence of these debris objects is the International Space Station (ISS), which had to perform five collision avoidance maneuvers in 2014. This has been the highest number of avoidance maneuvers recorded since 1998.[1] On July 16, 2015 the ISS crew were forced to scramble to safety in the Soyuz escape capsule after NASA received data on a fast approaching space debris object. The data regarding the debris being in close proximity, and on a highly probable collision course with the ISS, was received late and was imprecise as well. Hence the ISS could not make any evasive maneuvers. Close collision encounters not only endanger humans lives but pose a major threat to the many functional spacecraft and scientific equipment present in space. This makes it imperative to effectively study and develop methods for information fusion and RSO association to improve SSA.

The primary step in resolving the ever growing issue of space debris is proper association and identification of RSOs. Typically, RSOs are identified by matching sensor measurements (e.g. space-surveillance telescope data) to a space object catalog of previously identified objects. If the current RSO cannot be matched with any cataloged object, then that object is deemed an unidentified object, otherwise known as an "uncorrelated track," which is placed in the catalog and monitored throughout its entire life span if possible. Note that some agencies require that the object be determined all the way back to its launch origin to be identified. A catalog is simply a directory of objects that includes information pertaining to the object's estimated position and characteristics, such as the ballistic coefficient-like term found in two-line elements. The process of matching sensor measurements to a target, or RSO, is known as data association. It is important to note that an associated object may not be an identified object. Data association is fundamental in determining which RSOs within a sensor's field-of-view (FOV) are cataloged, and which are previously unidentified objects. An accurate and up-to-date RSO catalog is critical in avoidance maneuver planning and overall SSA.[2]

Much work has been done in the area of identification and data association in the recent years. These can be broadly divided into Gaussian and non-Gaussian methods. A covariance-based track association approach is shown in Ref. 3. An entropy-based data association approach for non-Gaussian probability density functions (pdfs) is shown in Ref. 4. Tracking multiple number of objects using finite-set statistics and finite mixture-model representations of multi-object pdfs is developed in Ref. 5. A Gaussian mixture Probability Hypothesis Density filter for multiple space object tracking is presented in Ref. 6. The ∂-General Labeled Multi-Bernoulli filter has been studied for tracking a large number of objects in Ref. 7. The use of magnetometers in identifying space objects in geosynchronous orbits has been studied and discussed in Ref. 8. Each of the aforementioned algorithms has its advantages and disadvantages. For example, Gaussian-based approaches may not work well when the pdf is non-Gaussian, and non-Gaussian approaches may be computationally expensive and also overburdensome when Gaussian pdfs exist.

The work presented here provides an alternate RSO data association approach, which has its roots in star pattern recognition.[9] Pattern recognition is a mature subject in the functionality of star trackers. A star tracker is an optical device, which collects star measurements in order to determine the attitude of its host spacecraft. One way stars are identified is by comparing the angles between observed stars in the star tracker's FOV with angles stored in a star catalog. This identification process is known as the angle method. If the angles of the observed stars match the angles of a set of stars in the catalog, then the spacecraft's attitude can be determined. Given the criticality of attitude knowledge to the performance of a spacecraft, the primary step is to consistently identify stars within the star tracker's FOV without requiring significant computation effort. The additional work on pattern recognition has led to the development of a method that uses planar triangle properties for spacecraft attitude determination in lieu of the angle method. This method is called the "Planar Triangle Method" (PTM).[10] The PTM is shown to be an accurate and efficient method of pattern recognition, and has been proven to work very well for spacecraft attitude determination. Pattern recognition algorithms attempt to match measurements with a certain target by using geometric data analysis. Given a cluster of data and stored *a priori* knowledge of the suspected targets, it is anticipated that this data will maintain a specific pattern that can be associated with the assigned targets. This work uses the PTM as an effective pattern recognition method for effective RSO data association.

Data association is the process of matching an unknown measured object to its known truth. Problems attributed to associating the true object from a cluster of similar objects can be addressed by various methods. These problems have been very well studied for the case of target tracking and multiple target tracking.[11] Data association has been studied in detail for target tracking in surveillance systems employing one or more sensors. In particular, many algorithms such as nearest neighbor, global nearest neighbor, multiple hypothesis tracking, joint probabilistic data association have been extensively studied.[11] Coupling traditional data association techniques with other methods for SSA is the focus of this work. In this paper traditional data association methods, such as elliptical/validation gates, are used to improve the association of the RSO when combined with the PTM. In traditional star identification algorithms, the errors in the reference vector are orders of magnitude smaller than the focal-plane errors, so that reference errors can be ignored in the pattern recognition algorithm. Here, errors in the RSO position significantly contribute to the overall uncertainty of the observation-to-truth correlation.

The outline of this paper proceeds as follows. First, the dynamics and measurement models are reviewed. Then, the PTM and traditional data association methods are discussed, as well as their combination for the RSO data association problem. Next, simulation results are presented for both uncluttered and cluttered environments. Finally, conclusions are drawn upon the simulation results.

II. Dynamics and Measurement Models

This section briefly covers the RSO dynamics model, as well as the focal-plane sensor model used for telescopes. A derivation of the errors induced on the focal-plane measurements due to RSO estimation errors is also shown. There are many forces acting on an RSO that perturb it away from the nominal orbit. These perturbations, or variations in the orbital elements, can be classified based on how they affect the Keplerian elements. The three basic type of orbital perturbations are secular variations, short period variations and long period variations. Secular variations have a long term linear variation on the orbit prediction, they cause the orbital elements to increase or decrease as time progresses. The main types of perturbation faced by a body in space are third-body perturbations, atmospheric drag, J_2 perturbations, solar radiation pressure, etc. Here, only J_2 perturbations are considered. The gravity potential for an arbitrary body is expressed as[12]

$$V(r,\phi) = -\frac{Gm}{r}\left[1 - \sum_{k=2}^{\infty}\left(\frac{r_{\text{eq}}}{r}\right)^k J_k P_k(\sin\phi)\right] \tag{1}$$

where G is gravitational constant, m is mass of the body, r_{eq} is the equatorial radius of the body, r is the distance to a point away from the body, J_k is the k^{th} zonal gravitational harmonic, P_k is the k^{th} order Legendre polynomial, and ϕ is the elevation angle of the vector tracking a point away from the body. The perturbing acceleration due to J_2 harmonics is given by

$$\mathbf{a}_{J_2} = -\frac{3}{2}J_2\left(\frac{\mu_g}{r^2}\right)\left(\frac{r_{\text{eq}}}{r}\right)^2 \begin{pmatrix} \left(1-5\left(\frac{z}{r}\right)^2\right)\frac{x}{r} \\ \left(1-5\left(\frac{z}{r}\right)^2\right)\frac{y}{r} \\ \left(3-5\left(\frac{z}{r}\right)^2\right)\frac{z}{r} \end{pmatrix} \tag{2}$$

The dynamics model for the i^{th} RSO is given by

$$\ddot{\mathbf{r}}_i^{\text{RSO}} = -\frac{\mu}{r_i^3}\mathbf{r}_i^{\text{RSO}} + \mathbf{a}_{J_2 i} \tag{3}$$

where $\mu = Gm$, $\mathbf{r}_i^{\text{RSO}} = [x_i\ \ y_i\ \ z_i]^T$ and $r_i = \|\mathbf{r}_i^{\text{RSO}}\|$.

Unit vector observations are assumed here. Focal-plane detectors form measurements according to a set of *collinearity equations*, which are standard in many photogrammetry applications.[13] Assuming that the camera boresight is aligned with the z-axis, these are given by

$$\alpha_i = -f\frac{A_{11}(x_i - X) + A_{12}(y_i - Y) + A_{13}(z_i - Z)}{A_{31}(x_i - X) + A_{32}(y_i - Y) + A_{33}(z_i - Z)}, \qquad i = 1, 2, \ldots, N \tag{4a}$$

$$\beta_i = -f\frac{A_{21}(x_i - X) + A_{22}(y_i - Y) + A_{23}(z_i - Z)}{A_{31}(x_i - X) + A_{32}(y_i - Y) + A_{33}(z_i - Z)}, \qquad i = 1, 2, \ldots, N \tag{4b}$$

where f is the focal length, $(X, Y\, Z)$ is the sensor (instrument) coordinates, denoted in vector form by $\mathbf{r}^{\text{INSTR}} = [X\ \ Y\ \ Z]^T$, and A_{ij} are the elements of the attitude matrix, which is a proper orthogonal 3×3 matrix, denoted by A. This matrix is given by three succussive rotations, given by

$$A = A_{\mathcal{T}/\mathcal{U}}\, A_{\mathcal{U}/\mathcal{F}}\, A_{\mathcal{F}/\mathcal{I}} \tag{5}$$

where $\mathcal{T}$ denotes the Instrument (INSTR) coordinate system, $\mathcal{U}$ denotes the local East-North-Up (ENU) coordinate system, $\mathcal{F}$ denotes Earth-Centered Earth-Fixed (ECEF) coordinate system, and $\mathcal{I}$ Earth-Centered Inertial (ECI) coordinate system. The ENU coordinate system is formed by a plane tangent to Earth's surface at a specific location. The origin of the tangent plane is usually dictated by the geolocation of a radar, telescope, or other instrument. Conversions between the various frames can be found in Ref. 14.

The observation vector that is directly measured by the instrument is

$$\boldsymbol{\gamma}_i \equiv \begin{bmatrix} \alpha_i \\ \beta_i \end{bmatrix} \tag{6}$$

and the corresponding measurement equation with noise is

$$\tilde{\boldsymbol{\gamma}}_i = \boldsymbol{\gamma}_i + \mathbf{w}_i \tag{7}$$

The zero-mean Gaussian noise process $\mathbf{w}_i$ is assumed to have covariance given by

$$R_i^{\text{FOCAL}} = \frac{\sigma^2}{1 + d\left(\alpha_i^2 + \beta_i^2\right)} \begin{bmatrix} \left(1 + d\alpha_i^2\right)^2 & \left(d\alpha_i\beta_i\right)^2 \\ \left(d\alpha_i\beta_i\right)^2 & \left(1 + d\beta_i^2\right)^2 \end{bmatrix} \tag{8}$$

where d is on the order of one (and often simply set to one) and σ is assumed to be known.[15]

In unit vector form, the observations are

$$\mathbf{b}_i = A\mathbf{r}_i, \qquad i = 1, 2, \ldots, N \tag{9}$$

where

$$\mathbf{b}_i \equiv \frac{1}{\sqrt{f + \alpha_i^2 + \beta_i^2}} \begin{bmatrix} -\alpha_i \\ -\beta_i \\ f \end{bmatrix} \tag{10a}$$

$$\mathbf{r}_i \equiv \frac{1}{\sqrt{\left(x_i - X\right)^2 + \left(y_i - Y\right)^2 + \left(z_i - Z\right)^2}} \begin{bmatrix} x_i - X \\ y_i - Y \\ z_i - Z \end{bmatrix} \tag{10b}$$

The measurement equation for the unit vector is

$$\tilde{\mathbf{b}}_i = \mathbf{b}_i + \boldsymbol{\upsilon}_i, \qquad \boldsymbol{\upsilon}_i^{\text{T}}\mathbf{b}_i = 0 \tag{11}$$

where the statistics of the noise $\boldsymbol{\upsilon}_i$ are given by

$$\text{E}\{\boldsymbol{\upsilon}_i\} = \mathbf{0} \tag{12a}$$

$$R_i^{\text{QUEST}} \equiv \text{E}\left\{\boldsymbol{\upsilon}_i\boldsymbol{\upsilon}_i^{\text{T}}\right\} = \sigma^2\left(I_{3\times3} - \mathbf{b}_i\mathbf{b}_i^{\text{T}}\right) \tag{12b}$$

where $I_{3\times3}$ is a 3×3 identity matrix. The QUEST measurement model[16] of Eq. (12b) makes the generally reasonable assumption that the uncertainty in the line-of-sight (LOS) unit vector measurement lies in the tangent plane to the unit sphere at the point where it intersects the measurement. This assumption becomes less valid for sensors with a wide FOV and LOS vectors far from the boresight direction.

To derive a wide-FOV covariance model, the 2×2 covariance R_i^{FOCAL} from Eq. (8) is transformed to a rank-deficient 3×3 covariance matrix (R_i^{wFOV}) via the Jacobian:[17]

$$J_i \equiv \frac{\partial\mathbf{b}_i}{\partial\boldsymbol{\gamma}_i} = \frac{1}{\sqrt{f + \alpha_i^2 + \beta_i^2}} \begin{bmatrix} -1 & 0 \\ 0 & -1 \\ 0 & 0 \end{bmatrix} - \frac{1}{f + \alpha_i^2 + \beta_i^2}\mathbf{b}_i\begin{bmatrix} \alpha_i & \beta_i \end{bmatrix} \tag{13}$$

With this J_i, the new covariance is given by

$$R_i^{\text{wFOV}} = J_i R_i^{\text{FOCAL}} J_i^{\text{T}} \tag{14}$$

Reference 18 proves that the wide-FOV covariance model achieves the Cramér-Rao lower bound. Thus, this covariance model is used for the work presented here, which is denoted by R_i^{INSTR}.

The main difference between star tracker applications and RSO tracking applications is that the reference vector $\mathbf{r}_i$ contains errors that cannot be ignored in general for the RSO case. It is assumed that the error-covariance of the i^{th} RSO estimate, denoted by $\hat{\mathbf{r}}_i^{\text{RSO}}$ which is computed from an orbit determination process, is given by R_i^{RSO}. The vector $\mathbf{r}_i$ can be rewritten as

$$\mathbf{r}_i = \frac{\mathbf{r}_i^{\text{RSO}} - \mathbf{r}^{\text{INSTR}}}{\|\mathbf{r}_i^{\text{RSO}} - \mathbf{r}^{\text{INSTR}}\|} \tag{15}$$

Its corresponding estimate is computed by

$$\hat{\mathbf{r}}_i = \frac{\hat{\mathbf{r}}_i^{\text{RSO}} - \mathbf{r}^{\text{INSTR}}}{\|\hat{\mathbf{r}}_i^{\text{RSO}} - \mathbf{r}^{\text{INSTR}}\|} \tag{16}$$

Taking the partial of Eq. (15) with respect to $\mathbf{r}_i^{\text{RSO}}$ gives

$$\mathcal{J}_i \equiv \frac{\partial \mathbf{r}_i}{\partial \mathbf{r}_i^{\text{RSO}}} = \frac{1}{\|\mathbf{r}_i^{\text{RSO}} - \mathbf{r}^{\text{INSTR}}\|} I_{3\times 3} - \frac{\left(\mathbf{r}_i^{\text{RSO}} - \mathbf{r}^{\text{INSTR}}\right)\left(\mathbf{r}_i^{\text{RSO}} - \mathbf{r}^{\text{INSTR}}\right)^T}{\|\mathbf{r}_i^{\text{RSO}} - \mathbf{r}^{\text{INSTR}}\|^3} \tag{17}$$

Note that $\mathbf{r}^{\text{INSTR}}$ is constant and is assumed to be well known. It is assumed here that the current $\tilde{\mathbf{b}}_i$ is not used to determine $\hat{\mathbf{r}}_i^{\text{RSO}}$, so that no correlations exist between the estimate and the measurement. This is practically true because the RSO estimates are obtained by propagating the dynamics model along with its error-covariance from a previous time to the time of the instrument sighting. Therefore, since the errors between the focal plane and RSO positions are uncorrelated the total covariance accounting for both errors is simply given by

$$R_i = R_i^{\text{INSTR}} + A\,\mathcal{J}_i R_i^{\text{RSO}} \mathcal{J}_i^T A^T \tag{18}$$

The attitude matrix is used to map the RSO covariance into the instrument coordinate system. Also, note that R_i contains true values of the focal plane observations and true values of the RSO position. These can be replaced with their corresponding measurements or estimates, which leads to second-order error effects in the computation of R_i.

III. Planar Triangle Method

The planar triangular method and the spherical triangular methods (STM) are both pattern recognition algorithms initially applied for star identification. These methods are extensions to the popular angle method, which requires two vectors while the STM and PTM require at least three vectors. The novelty lies in the fact that the STM and PTM require less pivoting, and provide a more consistent solution when compared to the angle method for pattern recognition. In this paper, details about the PTM are shown. Details of the STM can be found in Ref. 19. For a complete derivation of the PTM refer to Ref. 10. It has been determined in Ref. 10 that the PTM yields similar performance to that of the STM. Therefore, the PTM is preferred over STM due to reduced complexity and computational cost. The PTM requires that there be at least three objects present in the FOV. Again, it will be necessary to introduce pivoting with the PTM to reduce multiple solutions.

The PTM works on an elementary concept of pattern recognition, i.e. pattern matching for data association of RSOs. The PTM uses the objects present in the FOV to form triangles from which the area and polar moment of the triangles are then calculated. The catalog is then searched for matching areas and polar moments. If multiple matches are found, then one of the vertices of the triangle is pivoted using another star. This process is continued until a single solution can be reached. For the purpose of matching objects in the FOV with that of the ones present in the catalog, the PTM exploits information using some simple geometrical properties of triangles.

The two properties used by the PTM to identify the objects in the FOV are area and polar moment of the planar triangles. The area of the planar triangle can be given by the Heron's formula.[10] Given three unit vectors pointing toward three space objects, denoted by $\tilde{\mathbf{b}}_1$, $\tilde{\mathbf{b}}_2$ and $\tilde{\mathbf{b}}_3$, the area of a planar triangle is given by

$$\mathcal{A} = \sqrt{s\,(s-a)\,(s-b)\,(s-c)} \tag{19}$$

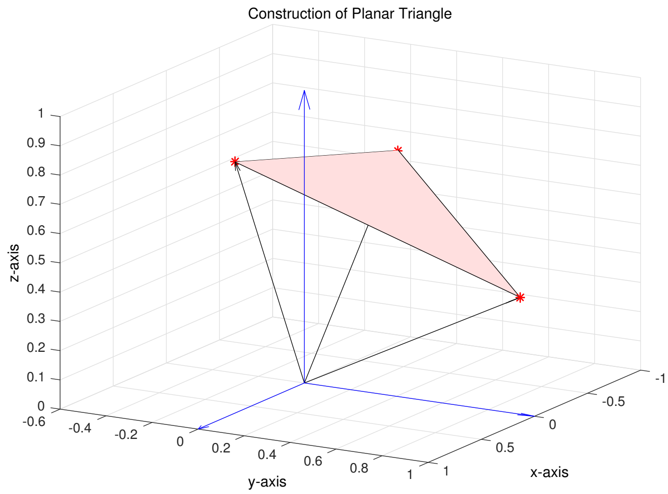

Figure 1. Planar Triangles Formed with Three Objects

where

$$s = \frac{1}{2}(a + b + c) \tag{20a}$$

$$a = ||\tilde{\mathbf{b}}_1 - \tilde{\mathbf{b}}_2|| \tag{20b}$$

$$b = ||\tilde{\mathbf{b}}_2 - \tilde{\mathbf{b}}_3|| \tag{20c}$$

$$c = ||\tilde{\mathbf{b}}_1 - \tilde{\mathbf{b}}_3|| \tag{20d}$$

A depiction of the planar triangle between three unit vectors is shown in Figure 1. In practice, the three unit position vectors contain sensor error. Therefore, an expression for the standard deviation of the planar triangle area is desired. Since Eq. (19) is nonlinear, a linearization technique, similar to how Eq. (14) is derived, is used to extract the variance of the area.

To compute this variance the following 1×9 partial derivative matrix is evaluated:

$$H = \begin{bmatrix} \mathbf{h}_1^T & \mathbf{h}_2^T & \mathbf{h}_3^T \end{bmatrix} \tag{21}$$

where

$$\mathbf{h}_1^T \equiv \frac{\partial \mathcal{A}}{\partial a}\frac{\partial a}{\partial \mathbf{b}_1} + \frac{\partial \mathcal{A}}{\partial c}\frac{\partial c}{\partial \mathbf{b}_1} \tag{22a}$$

$$\mathbf{h}_2^T \equiv \frac{\partial \mathcal{A}}{\partial a}\frac{\partial a}{\partial \mathbf{b}_2} + \frac{\partial \mathcal{A}}{\partial b}\frac{\partial b}{\partial \mathbf{b}_2} \tag{22b}$$

$$\mathbf{h}_3^T \equiv \frac{\partial \mathcal{A}}{\partial b}\frac{\partial b}{\partial \mathbf{b}_3} + \frac{\partial \mathcal{A}}{\partial c}\frac{\partial c}{\partial \mathbf{b}_3} \tag{22c}$$

The partials with respect to a, b and c are given by

$$\frac{\partial \mathcal{A}}{\partial a} = \frac{u_1 - u_2 + u_3 + u_4}{4\mathcal{A}} \tag{23a}$$

$$\frac{\partial \mathcal{A}}{\partial b} = \frac{u_1 + u_2 - u_3 + u_4}{4\mathcal{A}} \tag{23b}$$

$$\frac{\partial \mathcal{A}}{\partial c} = \frac{u_1 + u_2 + u_3 - u_4}{4\mathcal{A}} \tag{23c}$$

where

$$u_1 = (s-a)(s-b)(s-c) \tag{24a}$$
$$u_2 = s(s-b)(s-c) \tag{24b}$$
$$u_3 = s(s-a)(s-c) \tag{24c}$$
$$u_4 = s(s-a)(s-b) \tag{24d}$$

The partials with respect to $\mathbf{b}_1$, $\mathbf{b}_2$ and $\mathbf{b}_3$ are given by

$$\frac{\partial a}{\partial \mathbf{b}_1} = (\mathbf{b}_1 - \mathbf{b}_2)^T/a, \quad \frac{\partial a}{\partial \mathbf{b}_2} = -\frac{\partial a}{\partial \mathbf{b}_1} \tag{25a}$$
$$\frac{\partial b}{\partial \mathbf{b}_2} = (\mathbf{b}_2 - \mathbf{b}_3)^T/b, \quad \frac{\partial b}{\partial \mathbf{b}_3} = -\frac{\partial b}{\partial \mathbf{b}_2} \tag{25b}$$
$$\frac{\partial c}{\partial \mathbf{b}_1} = (\mathbf{b}_1 - \mathbf{b}_3)^T/c, \quad \frac{\partial c}{\partial \mathbf{b}_3} = -\frac{\partial c}{\partial \mathbf{b}_1} \tag{25c}$$

The variance of the area, denoted by $\sigma_{\mathcal{A}}^2$, is given by

$$\sigma_{\mathcal{A}}^2 = H\,R\,H^T \tag{26}$$

where

$$R \equiv \begin{bmatrix} R_1 & 0_{3\times3} & 0_{3\times3} \\ 0_{3\times3} & R_2 & 0_{3\times3} \\ 0_{3\times3} & 0_{3\times3} & R_3 \end{bmatrix} \tag{27}$$

where $0_{3\times3}$ denotes a 3×3 matrix of zeros and R_1, R_2 and R_3 are given by Eq. (18). Note that the matrices H and R are evaluated at the respective true values; however, replacing the true values with the measured ones leads to second-order errors that are negligible. Since the standard deviation, $\sigma_{\mathcal{A}}$, is derived analytically, the bounds over which the true area is likely to exist can be determined precisely to within any prescribed confidence level, no matter the shape or size of the planar triangle.

The triangular polar moment of inertia is introduced as a supplemental screening property to the planar triangle area. If two planar triangles have the same area, then their polar moments are most likely different. The reverse is also true; if two planar triangles have the same polar moments, then it is likely that their areas are not equal. The polar moment of inertia property helps further differentiate possible triangle combinations. The polar moment of inertia the planar triangle is given by

$$\mathcal{J} = \mathcal{A}\,(a^2+b^2+c^2)/36 \tag{28}$$

As with the area, the variance of the polar moment of inertia can also be derived in closed form. To compute this quantity the following 1×9 partial derivative matrix is evaluated:

$$\bar{H} = \begin{bmatrix} \bar{\mathbf{h}}_1^T & \bar{\mathbf{h}}_2^T & \bar{\mathbf{h}}_3^T \end{bmatrix} \tag{29}$$

where

$$\bar{\mathbf{h}}_1^T \equiv \frac{\partial \mathcal{J}}{\partial a}\frac{\partial a}{\partial \mathbf{b}_1} + \frac{\partial \mathcal{J}}{\partial c}\frac{\partial c}{\partial \mathbf{b}_1} + \frac{\partial \mathcal{J}}{\partial \mathcal{A}}\mathbf{h}_1^T \tag{30a}$$
$$\bar{\mathbf{h}}_2^T \equiv \frac{\partial \mathcal{J}}{\partial a}\frac{\partial a}{\partial \mathbf{b}_2} + \frac{\partial \mathcal{J}}{\partial b}\frac{\partial b}{\partial \mathbf{b}_2} + \frac{\partial \mathcal{J}}{\partial \mathcal{A}}\mathbf{h}_2^T \tag{30b}$$
$$\bar{\mathbf{h}}_3^T \equiv \frac{\partial \mathcal{J}}{\partial b}\frac{\partial b}{\partial \mathbf{b}_3} + \frac{\partial \mathcal{J}}{\partial c}\frac{\partial c}{\partial \mathbf{b}_3} + \frac{\partial \mathcal{J}}{\partial \mathcal{A}}\mathbf{h}_3^T \tag{30c}$$

with

$$\frac{\partial \mathcal{J}}{\partial a} = \mathcal{A}\,a/18, \quad \frac{\partial \mathcal{J}}{\partial a} = \mathcal{A}\,b/18, \quad \frac{\partial \mathcal{J}}{\partial a} = \mathcal{A}\,c/18 \tag{31a}$$
$$\frac{\partial \mathcal{J}}{\partial \mathcal{A}} = (a^2+b^2+c^2)/36 \tag{31b}$$

All other quantities in Eq. (30) are given from the area variance calculations. The variance of the polar moment of inerita, denoted by $\sigma^2_{\mathcal{J}}$, is given by

$$\sigma^2_{\mathcal{J}} = \bar{H}\, R\, \bar{H}^T \tag{32}$$

As with the area variance, the true values are replaced with the respective measured polar moment of inertia.

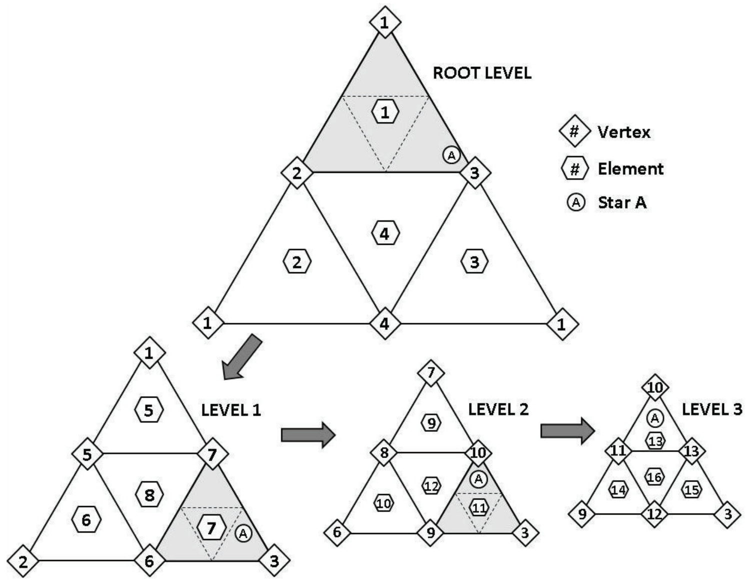

Figure 2. Flattened Spherical Quad-Tree Structure

A. Planar Triangle Catalog

It is necessary to organize the planar triangle catalog in an efficient manner to help reduce search and creation time. This is especially important because, unlike stars, RSO catalogs are updated frequently (sometimes daily). Therefore, a new planar triangle catalog will need to be created once an RSO catalog is made available. In order to make the catalog easily accessible, a spherical quad-tree structure is used. The spherical quad-tree structure is similar to a traditional quad-tree structure except it uses spherical triangles instead of square quadrants as the element type. The traditional quad-tree is presented in detail in Ref. 19. A spherical quad-tree structure is a multi-level apportioned spherical triangle that enables objects to be associated based on their location within that spherical triangle. If the spherical triangle is flattened in 2-D space, then it would somewhat resemble the triangular structure shown in Figure 2. The spherical triangle is divided into four labeled elements in each of its three levels. Also, each individual element is assigned three labeled vertices. During the spherical quad-tree build, each object is assigned to a spherical triangle and the associated elements based on its location in the celestial sphere. The elements and vertices are the parameters used to locate a particular object in the structure. There are four spherical triangles that create a spherical tetrahedron that spans the entire celestial sphere. To further simplify the search, only the objects within the specified FOV are considered. Therefore, any object outside this boundary is omitted from the search.

During a search it is not immediately known where each object is located since there are a significant number of them cataloged. To clarify the search process, an example will be presented. Assume that any object in space, denoted as star A in Figure 2, is the only object cataloged, and it is located inside root (top level) – element 1, level 1 – element 7, level 2 – element 11, and level 3 – element 13. Now, suppose measurements are taken and the measured angle lies within a boundary of the spherical triangle, say the lower right of element 1. Considering more levels, the measured angle is determined to lie within element 13. Since star A is contained in element 13, star A is the measured object. If the measured angle lies within a different boundary and other objects are cataloged, then a different object may be identified. Clearly, it is necessary to define multiple levels in order to obtain a sufficient amount of precision when the number of objects is large. The benefit of the spherical quad-tree structure is that once it is created, an object can be identified without using any information about the unit position vector of the object.

The spherical quad-tree is an efficient way to store information, but an optimal organization of the catalog is desired. If the catalog can be organized in such a way that it follows a mathematical equation, then it would be simple to find a particular property in the catalog. For example, if it is determined that the planar triangle area is within a certain boundary, then a search of the catalog for that boundary would be required. If the catalog is not organized appropriately, then it would result in a search spanning the majority of the catalog. Since the catalog can be quite extensive, this would lead to a high computation cost. To resolve this issue the k-vector approach[20] is used. For object pattern recognition, if the area of each pair of objects is plotted against its location in the catalog, then a line can be drawn connecting the first and last pair of objects. The equation of this line can be used in association with the generated k-vector to locate where in the catalog a particular pair of objects with a given angle is located. This greatly reduces the computational burden since the object pattern search algorithm requires a search of the pairs of objects only within a measurement uncertainty region, not a search of the entire catalog. For the planar triangle approach a parabolic k-vector is constructed because it is the best relationship between the planar triangle identifier and the planar triangle area. If a certain planar triangle area is desired, then the k-vector will quickly provide the associated planar triangle identifier.

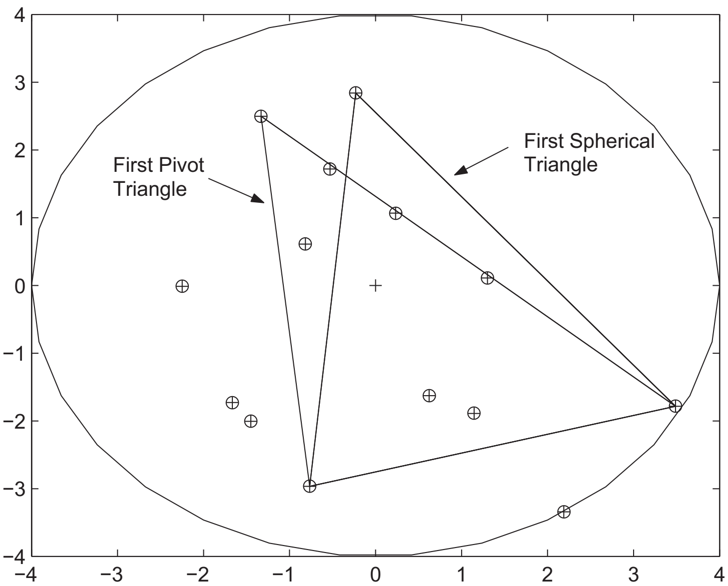

Figure 3. Pivoting within Field of View

B. Planar Triangle Pivot

If several objects are within the FOV, then it is likely that there can be multiple solutions to the search. To reduce and ultimately eliminate multiple solutions, planar triangle pivoting is leveraged. The method for pivoting planar triangles is similar to the method for pivoting angles using two objects. A planar triangle is made from three objects in the FOV, and its area and polar moment of inertia are calculated. A range over which the true area and polar moment of inertia exist are calculated using the standard deviations for each. Going through the catalog, triangles that have an area and polar moment that fit within the bounds calculated for the triangle in the FOV are sought. Ideally, only one possible solution exists, but this is typically unlikely. When more than one solution exists, a pivot is performed. Another planar triangle is made from the objects in the FOV such that there are two objects in common with the first triangle, as shown in Figure 3. A list of possible solutions is made, and then the solutions between the first planar triangle and second planar triangle are compared. Any solution in each list that does not have two objects in common with at least one solution in the other lists is discarded. After the comparison is made, if more than one solution exists, then another pivot is made. Pivoting continues until either a single solution is found or the pivoting limit has been met. Pivoting such that only one object is shared between the first and second planar triangles can be done, but would be less effective. The number of triangles that are likely to share one object is greater than two, so the solution would require a greater number of pivots.

Also considering false objects and highly cluttered object patterns, the pivoting order would ideally pivot away from objects that are uncertain. This concept becomes feasible with the addition of the gating method results. Careful ordering of the pivoting of the objects in the FOV allows the PTM to strategically pick the next object to pivot.

IV. Traditional Data Association Methods

Nearest Neighbor (NN) is the simplest data association algorithm, used for single target tracking. When multiple measurements fall within a target's validation gate, the one that is closest with respect to a predefined distance measure is assumed to come from that target. Sometimes called the optimal assignment approach, global nearest neighbor (GNN) is the multi-target version of the NN approach. Instead of minimizing a single distance, GNN looks to minimize a global distance measure. Two assumptions are made: 1) each measurement can only be associated to one track, and 2) each track can only be associated with one measurement. The primary advantage of the GNN algorithm is that its computational cost does not increase rapidly as the number of targets increases. The disadvantage of this algorithm is that track initiation must be performed separately. Reference 21 identifies two classes of track initiation techniques: sequential and batch. The former is preferred for low-clutter environments, while the latter is used for high-clutter environments. The primary difference between the two is that batch techniques are generally slower and more computationally expensive.

The goal of this work is to associate RSOs within a single object field observation. For this reason the NN approach is used as the data association method for gating. This helps to keep away any undesirable observation that might be made. A simple example of a gating method is that of a house with an automatic gate that opens only when the identity of the person at the gate can be verified. However, if the identity cannot be verified, then the person does not have access. Similarly, validation gates do not let the measurement be associated with the track if the measurement does not pass the gate provided by the truth and assumed uncertainty. A gate is formed about the predicted measurement, and all observations that fall within the gate are considered for the track update. The manner in which the observations are actually chosen to update the track depends on the data association method in use. Gating methods are useful for reducing complexity and increasing computational efficiency.

A. Elliptical Gates

The Mahalanobis distance is synonymous to the ellipsoidal gate. This is a statistical tool used to measure the distance between points in multivariate data. Mahalanobis distance measure is also the distance between a point P and a distribution D. The Mahalanobis distance was originally developed for use with multivariate normal distributed data. A prediction ellipse is a region for predicting the location of a new observation under the assumption that the population is bivariate normal. For example, an 80% prediction ellipse indicates a region that would contain about 80% of the new samples that are drawn from a bivariate normal population with mean and covariance matrices that are equal to the sample estimates. The Mahalanobis distance is also said to be the simple Euclidean distance, which takes into account the covariance of the data. If the covariance of the data is an identity matrix, then the Mahalanobis distance is equivalent to the Euclidean distance. The Mahalanobis distance measure used in this work is mathematically written as:

$$d_{ij} = \sqrt{\mathbf{e}_{ij}^T R_i^{-1} \mathbf{e}_{ij}} \tag{33}$$

where R_i is given by Eq. (18), and the residual $\mathbf{e}_{ij}$ is given by $\mathbf{e}_{ij} = \tilde{\mathbf{b}}_j - \hat{\mathbf{b}}_i$, with $\hat{\mathbf{b}}_i = A\hat{\mathbf{r}}_i$, where $\hat{\mathbf{r}}_i$ is given by Eq. (16). Note that d_{ij} is computed for all possible $(i,\, j)$ pairs. The Mahalanobis distance from Eq. (33) represents the general arbitrarily oriented ellipsoid. A ellipsoid with center at $\mathbf{v}$ is defined by solutions to $\mathbf{x}$ of the equation

$$(\mathbf{x} - \mathbf{v})^T Z (\mathbf{x} - \mathbf{v}) = 1 \tag{34}$$

where Z is a positive definite matrix. The equation of an ellipse given by Eq. (34) and the Mahalanobis distance are clearly identical in form, and hence the Mahalanobis distance is often referred to as either *elliptical gates* or *ellipsoidal gates*.

In the simplest of terms the Mahalanobis distance is a powerful method for measuring how similar some set of conditions are to an ideal set of conditions. This is precisely what is desired by the RSO data association problem, because it is desired to see how similar a point in space is to all true points in the catalog. Unlike the Euclidean distance the Mahalanobis distance takes into account the following facts:

- It accounts for the fact that the variance is different in each direction;
- It accounts for the covariance between variables;
- It reduces to the Euclidean distance for uncorrelated variables and unit variance.

It is desired to determine the probability that the measurement lies inside the following quadratic hyper-surface:

$$\mathbf{e}_{ij}^T R_i^{-1} \mathbf{e}_{ij} < \gamma^2 \tag{35}$$

The probability of a correct match is defined by the gate threshold γ. This area is called the validation gate, and the threshold value for γ can be obtained from the inverse χ^2 cumulative distribution. The solid ellipsoid of values satisfying

$$(\tilde{\mathbf{b}}_j - \hat{\mathbf{b}}_i)^T R_i^{-1} (\tilde{\mathbf{b}}_j - \hat{\mathbf{b}}_i) \le \chi_n^2(\alpha)$$

has probability $1 - \alpha$. For example, for three-variable vectors ($n = 3$), and $\alpha = 0.1$, then $\chi_n^2(\alpha) = 6.2513$, which is what is used in this work.

The Mahalanobis distance takes into account factors such as uncertainty and correlations between measurements. Therefore it is an effective tool to solve the RSO data association problem. It will also be shown that elliptical gates can be used to increase the performance of the PTM. This distance can be combined with algorithms such as the NN to associate closest neighbors in a multivariate data set. The NN maintains the single most likely hypothesis. The fundamental concept of the NN is to associate the most likely assignment of an measurement to its existing estimate. This association is attained by verifying if the measurement lies in the validation gate and it is the closest measurement to the existing estimate. The NN in the validation gate region is then assigned to the existing estimate, and this is updated.

The NN algorithm can be used with various types of distances (Euclidean, city block, Chebyshev, etc.). The most popular among these is the Mahalanobis distance or the ellipsoidal gate described in this section. The gate can be written in general by

$$G_r = \{\mathbf{z} : D(\mathbf{z}) \le \gamma\} \tag{36}$$

where $D(\mathbf{z})$ is the distance measure. For the RSO association problem the Mahalanobis distance is used as the distance measure. Also, $\mathbf{z}$ is the estimate, which is determined by propagating the state model of the target forward to the observation time. The measurements are associated to the estimates by the NN determination through

$$\mathbf{z}^* = \underset{\text{argmin}_j\, ij}{D}(\mathbf{z}), \quad j = 1, 2, \ldots, N \tag{37}$$

where N is the number of available observations. The subscripts i and j denote $\mathbf{e}_{ij}$ with corresponding R_i. Application of NN approach for RSO association when a measurement is available involves finding all the neighbors for a given measuremment. This measured value is then associated to the nearest vector in the data. This simple form of data association will be used for associating a single object to its true object. The NN approach can be implemented by the following algorithm:

1. Compute the Mahalanobis distance from all possible cataloged estimates to all measurements in the FOV;
2. Accept the closest measurement that passes the gate threshold;
3. Find the match with the lowest Mahalanobis distance for each estimate (ensure only one measurement is associated with each estimate);
4. Update the match as if it were the correct measurement.

V. Simulation Results

To simulate realistic conditions data from the debris field of the 2007 Chinese anti-satellite missile test of the Fengyun 1C satellite is used. This Chinese weather satellite was launched into a Sun-synchronous orbit with a mean altitude of 850 km and an inclination of 98.8 degrees.[22] The orbital elements of the 2,000 pieces of debris data for the Fengyun 1C are available on www.celestrak.com. Another set of 2,000 pieces of debris are also simulated to create a sufficient cluttered environment that stresses the data association algorithms.

The chosen site is the Ground-based Electro-Optical Deep Space Surveillance (GEODSS) instrument, which is located at the White Sands Missile Range in New Mexico. The location of the telescope is 32.82° latitude, −106.66° longitude and 1.250 (km) altitude. The simulated objects are normally distributed about the specific object in the Fengyun 1C debris field that has the smallest separation angle with respect to the normal vector of the site at a specific time. This provides a distribution of 2,000 simulated objects in which the majority are within the view of the site. In total, there are 4,000 RSOs that are cataloged and roughly 2,000 of those are in view of the site.

Simulated objects in ECI coordinates are shown in Figure 4. The ECI initial debris data are then propagated to obtain an instance of time in which there is an acceptable amount of debris visible to the site. Then the debris is converted to the ECEF coordinate system. To see RSOs in the FOV, transformations from ECEF to ENU to the INSTR frame are required. The reader is recommended to review Ref. 2 (chapter 5), for details of the simulations required to generate the RSO.

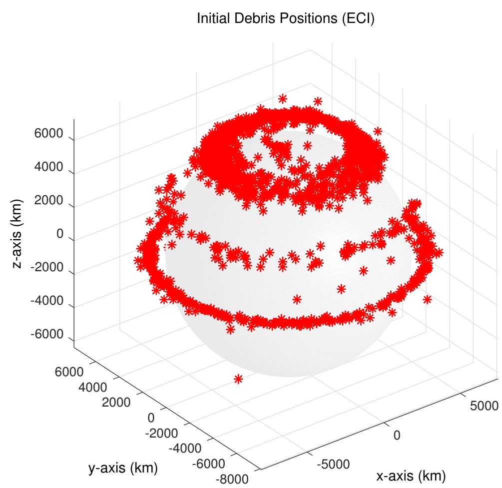

Figure 4. Debris in ECI Coordinate System

A. Planar Triangle Method Algorithm

The PTM code execution can be seen in Ref. 10. However a broad overview of the steps can be given as follows:

1. Create the spherical quad-tree structure;
2. Catalog planar triangles;
3. Add planar triangle properties;
4. Sort planar triangles;
5. Run the pattern recognition algorithm in a Monte Carlo regime.

The first step in the PTM code execution is to create a multi-level spherical quad-tree structure. Then, based on an RSO's position data, it is stored within that structure. Once all RSOs have been assigned a position in the tree structure, the planar triangle properties are computed and associated with that tree structure location. To increase efficiency further, a binary tree is implemented to sort the planar triangle properties according to the value of the planar triangle area. The ultimate goal is to provide an efficient storing mechanism that can be used to quickly associate an RSO based on planar triangle area and polar moment.

Once the storing mechanism (steps 1-4) has been constructed, it can now be used to compare focal-plane observations of RSOs from the catalog. Several Monte Carlo runs are executed to test the PTM. At each iteration, a random telescope boresight is generated, and an associated random INSTR frame is constructed. From this INSTR frame, all RSOs within the FOV are provided as inputs to the pattern recognition algorithm. This sequence is repeated many times in order to accumulate a large result set. A representation of the pattern recognition algorithm is as follows:

for $i = 1$ to number of desired iterations **do**

- Compute random boresight vector;
- Compute random INSTR frame with $\mathbf{t}_z$ aligned with boresight vector;
- Determine RSOs in FOV;
- Perform ENU to INSTR coordinate system transformation;
- Compute focal-plane observations;
- Add sensor error to focal-plane observations;
- Compute measured RSO position vectors with both measurement and sensor error;
- Compute planar triangle properties;
- Compute area variance;
- Compute polar moment variance;
- Compare computed values with catalog and determine matching RSOs.

The first step in the algorithm is to compute a random boresight vector. This represents a random telescope boresight, which is restricted to the physical attributes of the space surveillance telescope. The telescope is restricted to an elevation angle of 20 degrees above the horizon and an azimuth angle that spans the entire plane. Therefore the random boresight vectors are uniformly distributed within these boundaries. The random boresight vector is computed by

$$\theta_{\text{elev}} = \frac{\pi}{9} + \left[\frac{\pi}{2} - \frac{\pi}{9}\right] \texttt{rand}(1) \tag{38a}$$

$$\psi_{\text{az}} = 2\pi\, \texttt{rand}(1) \tag{38b}$$

$$\mathbf{r}_b = \begin{bmatrix} \cos(\theta_{\text{elev}})\cos(\psi_{\text{az}}) \\ \cos(\theta_{\text{elev}})\sin(\psi_{\text{az}}) \\ \sin(\psi_{\text{az}}) \end{bmatrix} \tag{38c}$$

In the above equation, θ_{elev} and ψ_{az} are the elevation and azimuth angles, respectively. The function `rand` is uniform random number generator. The random INSTR frame is then constructed with the $\mathbf{t}_z$ axis aligned with the current boresight vector.

The INSTR frame is constructed by:

$$\mathbf{t}_z = \mathbf{r}_b \tag{39a}$$

$$\mathbf{t}'_y = \mathbf{t}_z \times \mathbf{r}'_b \tag{39b}$$

$$\mathbf{t}_y = \frac{\mathbf{t}_z \times \mathbf{t}'_y}{\|\mathbf{t}_z \times \mathbf{t}'_y\|} \tag{39c}$$

$$\mathbf{t}_z = \frac{\mathbf{t}_y \times \mathbf{t}_z}{\|\mathbf{t}_y \times \mathbf{t}_z\|} \tag{39d}$$

where $\mathbf{r}'_b$ is a separate random vector generated from Eq. (38c), and $\mathbf{t}'_y$ is a temporary y-axis used to generate the orthogonality condition between $\mathbf{t}_z$ and $\mathbf{t}_y$. The specific orientation of the $\mathbf{t}_{xy}$ plane is not significant as long as $\mathbf{t}_z$ is along the boresight vector. The instrument is assumed to have a 6 degree FOV, which is represented by a plane at the end point of the random boresight vector. The condition for an object to be within the FOV is given by

$$\arccos(\mathbf{r}^{\mathrm{RSO}} \cdot \mathbf{r}_b) \leq \frac{3\pi}{180} \tag{40}$$

B. Execution of PTM

For the purpose of simulation 1,000 random boresight vectors are generated. The RSOs in the FOV for each boresight vector are calculated, and when the RSOs in FOV are more than the minimum number desired, the PTM is executed. Two Monte Carlo runs of random attitude tests (RATs) are performed − each Monte Carlo run consists of 1,000 RATs, and this Monte Carlo simulation is done two times for every case of measurement error. An illustration of the random boresight vectors computed with the debris can be seen in Figure 5, which gives a clear understanding of how the boresight vectors are generated, and also helps to visualize the RSOs that are within the FOV. In Figure 5 the red dots are the debris in space. The blue straight lines pointing up towards the debris are the boresight vectors of the telescope. The blue lines at the base of the boresight vectors show the other two axes of each boresight vector. The blue circular head on top of each boresight vector is the FOV for that particular telescope boresight, and the light pink triangles are the planar triangles formed between the debris pieces in space. For the purpose of simulations, six cases of measurement error are used listed in Table 1.

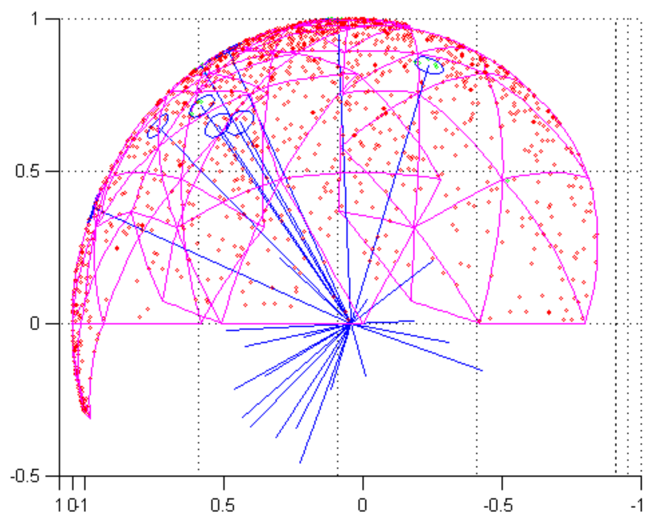

Figure 5. Random Attitude Tests with Debris

Table 1. Measurement Errors

Iteration no.	1	2	3	4	5	6
3σ errors (km)	0.06	0.12	0.24	0.3	0.6	0.9

C. Gating-Based Data Association

Gating-based data association involves the association of measurements to known true values or tracks, and the sorting of results based on the data association method. As mentioned the data association method for this simulation is the NN method. In order to evaluate the performance of this algorithm with respect to object association, randomly selected FOVs in the aforementioned object measurement and catalog are selected and used as an input to the gating method. Figure 6 shows the number of debris objects visible to the ground site for a representative single run. The Mahalanobis distance between each measured observation and all its true positions are found. Then the NN algorithm is used to associate the closest measured value to the true debris. Another logical check is performed to ensure that only one measurement is associated with a single track. If more than one association is made to a true track, then the measurement with the lowest Mahalanobis distance is chosen. At the output of each association, a check is performed to see if the associated objects match the true objects. If both the measured and truth are the same, then a correct match is counted and the truth counter is incremented, else a bad/fail counter is incremented.

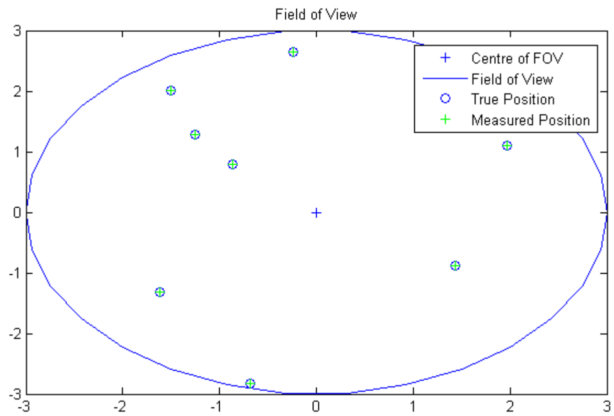

Figure 6. Debris in the FOV

D. Cluttering the FOV to Test Gating and PTM

Since the gating method performs exceptionally well in cases where the FOV is very lightly dense, the system is strained for cases where the FOV is very dense, or cluttered with debris. A function is used to artificially add pieces of debris in the FOV. To add closely spaced debris the pairwise distance between each piece of debris in the FOV is taken. The minimum distance in each case is taken and used as the 3σ (standard deviation) to generate three pieces of debris around each already existing debris to populate the FOV, as shown in Figure 7. This figure illustrates the cluttering approach used to demonstrate performance of the proposed algorithms. Once the addition of debris is done, the simple elliptical gating approach is used for the debris matching, and the results are saved accordingly.

VI. Gating-Assisted Planar Triangular Method

This method couples the working of the PTM and the gating method. First, the gating method is executed as a precursor to the PTM. Here, the gating method is used to associate the measured data to the truth data under varying measurement errors. Once gating data associations are completed, the PTM is executed using the updated track values determined in the gating process.

The pre-processing of the measurement field with the gating data association helps the PTM to compare debris pieces that are already associated to the truth. In the case where the gating process incorrectly matches a measurement to the wrong track, the PTM algorithm has additional criteria in the triangle properties to screen mismatches. The polar moment of inertia provides additional screening criteria to evaluate observations determined in the gating processing. When considering the flexibility to use the pivoting methods, the PTM acts as a robust additional screening method for gating results.

Additional performance can be realized by providing an intelligent pivoting order based on the output of the gating results. If there are sufficient gating-associated objects, then the combinations of associated objects are determined, and then they are sorted based on triangle area. The sorted results are re-organized to follow the traditional pivot method where one object of the triangle is shifted from the first to the next analysis. This approach allows the PTM to use more information yielded from gating to assist in determining precise and robust object association. If more pivots are available, then the objects in the FOV that are not associated by gating can fill out the remainder of the pivots. Along with the updated object vectors,

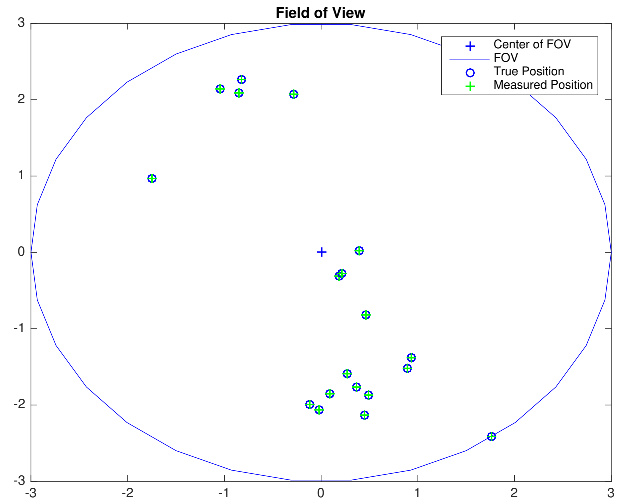

Figure 7. Adding Three Pieces of Debris Around Each Existing Piece to Clutter the Environment

the pre-sorted pivot list is handed over to the traditional PTM algorithm. Once the PTM is executed the results obtained are saved for each run. Results below show that this method increases the efficiency and effectiveness of the PTM under highly cluttered and uncertain conditions.

The gating-assisted PTM object association method is summarized as follows:

- Perform gating data association with measured objects in the FOV;
- Update measured tracks with associated vectors based on the output of the gating method;
- Determine triangles and planar triangle area based on the combinations of the observations;
- Sort the area of the triangles in descending order;
- Starting with the largest area, re-sort triangles based on pivoting logic used in the PTM approach;
- Using the pivoting list and updated track vectors, execute the PTM algorithm to determine object matches.

Outputting a failed result from the PTM given incorrectly associated objects in the gating pre-processing is almost as good as a correct output from the PTM. By signifying a failure given incorrect observations, the PTM acts as a screen previously unavailable to the gating method alone. Without the PTM addition, the gating method can supply incorrect matches without any additional checks.

By prioritizing the inputs of the PTM with the results of the gating method, notable improvements to the stand-alone performance of both algorithms are realized. The synergistic result of joining these two methods yields improvements than either alone. The PTM benefits from the prioritization of results from gating because it does not have to pivot through uncertain measurements. The gating method benefits from the robustness of the PTM because the PTM can correct and/or reject incorrect associations made from gating. The gating-assisted PTM is also shown to perform well under highly populated false object cases.

A. Results

The purpose of this work is to show that the accuracy of the PTM can be improved by using elliptical gates as a screening method to associate the measured observations to the truth. A comprehensive study has also been performed on using just the gating approach for data association. During the study it is found that the simple gating approach works well in cases where the FOV is not cluttered with debris and corrupted by uncertainty. The simple gating approach for an uncluttered FOV proves to have a better performance under varying uncertainty in the debris position, when compared to the PTM. But when left without additional screening, the gating method yields more incorrect associations.

Figure 8 shows the accuracy of the gating method compared to the PTM. Note that each run number represents 1,000 Monte Carlo runs. The gating method is very promising in an uncluttered regime, while both algorithms tend to be sensitive to measurement uncertainty. The uncluttered condition is useful as a baseline, but to stress the algorithms, the FOV is artificially cluttered with additional debris.

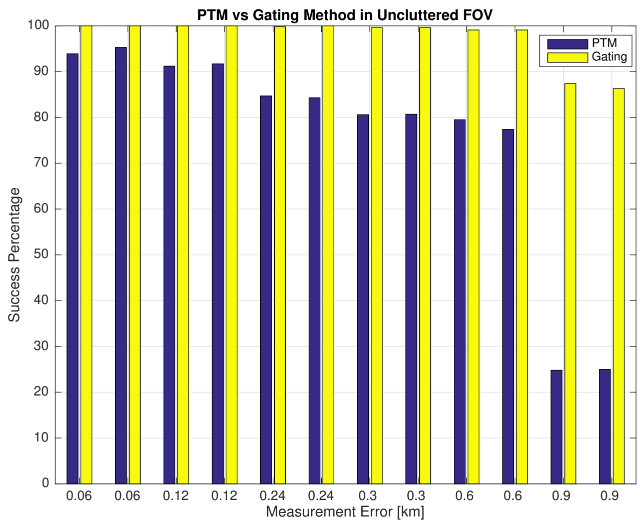

Figure 8. Accuracy of the Gating Method Compared to the PTM in an Uncluttered FOV

Table 2. x-Axis Run Number and Corresponding Measurement Error

Run No.	1, 2	3, 4	5, 6	7, 8	9, 10	11, 12
RSO Meas. 3σ Error (km)	0.06	0.12	0.24	0.3	0.6	0.9

The performance of the object association algorithms decrease when presented with a highly cluttered environment. As expected the accuracy of the gating method becomes more sensitive to noise as performance suffers with the increase in measurement uncertainty. As the measurement uncertainty ellipse and the tightly cluttered measurements start to overlap, the ability of either algorithm to associate the likely object drops significantly. The cluttered FOV case is run for both the gating and PTM algorithms, and results are compared. In Figure 9, the PTM results show significant sensitivity to the highest measurement case. Both algorithms take a hit to performance and show increased sensitivity to uncertainty.

To investigate the performance further, Figures 10(a) and 10(b) illustrate the minimum pairwise distance measured in each FOV run in the cluttered case where the respective algorithm fails to produce the correct object association. Clearly, the tightly spaced and cluttered FOV is the leading cause of failure in the two algorithms. The separation distance at which both algorithms degrade is well below the average distance measured in the FOV.

To improve upon the performance of the gating and PTM, the gating-assisted PTM is evaluated. As described above in Section VI, the gating-assisted PTM utilizes the gating algorithm as a precursor to the PTM. When this gating method is performed before the PTM, significant robustness to noise and uncertainty is shown. The results shown in Figure 11 show clear improvement of performance of the new method to that of the previously existing PTM or gating. It can be seen that the PTM with gates performs better than the PTM alone. The PTM with gating pre-processing shows an improvement over gating and PTM alone that gets better with increasing measurement uncertainty. To show the combined approach is statistically significant a hypothesis test is performed. In this method it is found that the null hypothesis shows the methods are identical in performance at the 99% confidence interval. After performing the hypothesis testing, the null hypothesis was rejected. This confirms the assumption that the application of gating to the PTM helps enhance the overall association performance.

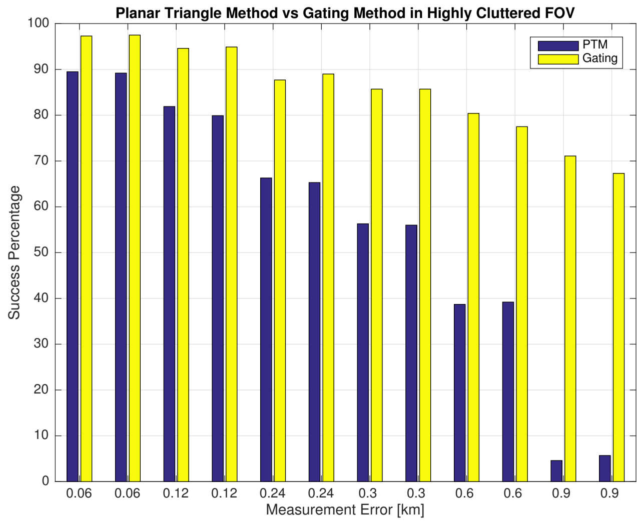

Figure 9. Comparision of PTM with the Gating Method for Varying Measurement Errors

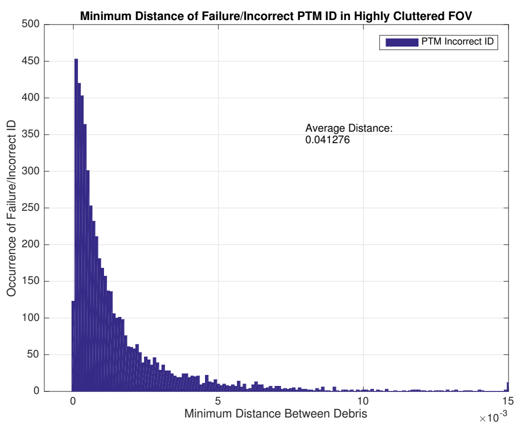

(a) **Min Distance of Failed Cases, PTM**

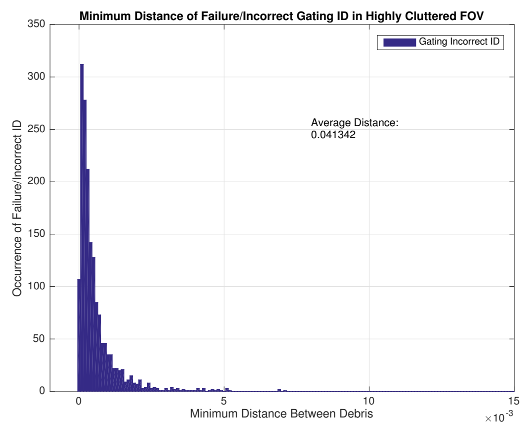

(b) **Min Distance of Failed Cases, Gating**

Figure 10. Minimum Distance Analysis for Failures on PTM and Gating Methods in Cluttered Environments

The breakdown of the gating-assisted PTM performance against incorrect associations from the gating pre-processing shows the power of pivoting and of the pre-sorted pivoting index. The inclusion of the PTM allows for a significant reduction in false associations when compared to the gating-only method. For all cases, the PTM is able to correct the incorrect gating associated measurements at a rate of over 95%. Figures 12(a) and 12(b) illustrate the performance of the gating-assisted PTM as well as how the algorithm handles incorrect associations from gating. The screening capability of the PTM significantly enhances the success rate of the output by utilizing the planar triangle properties as well as pivoting. The extremely small number of incorrectly associated object combinations outputted from the gating-assisted PTM is notable given the harsh cluttering and uncertainty condition. The ability to screen and remove bad associations is attributed to the PTM as demonstrated in Ref. 10.

To evaluate the performance of the proposed algorithm in yet another challenging environment, the clutter added to the FOV is not cataloged, therefore the clutter acts as false object observations. The false object could be an uncataloged star/object or a sensor malfunction. It is important to note that the approach in this work uses “static” (spatial) observations (i.e. one snapshot in the FOV), unlike “dynamic”

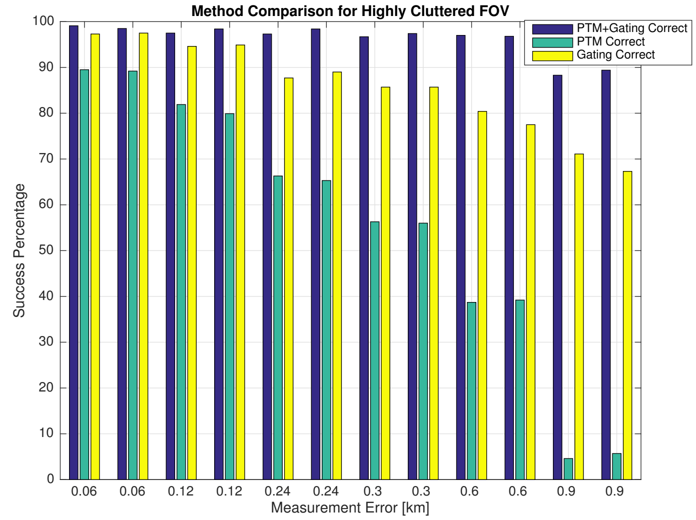

Figure 11. Performance of Gating-Assisted PTM in Highly Cluttered FOV

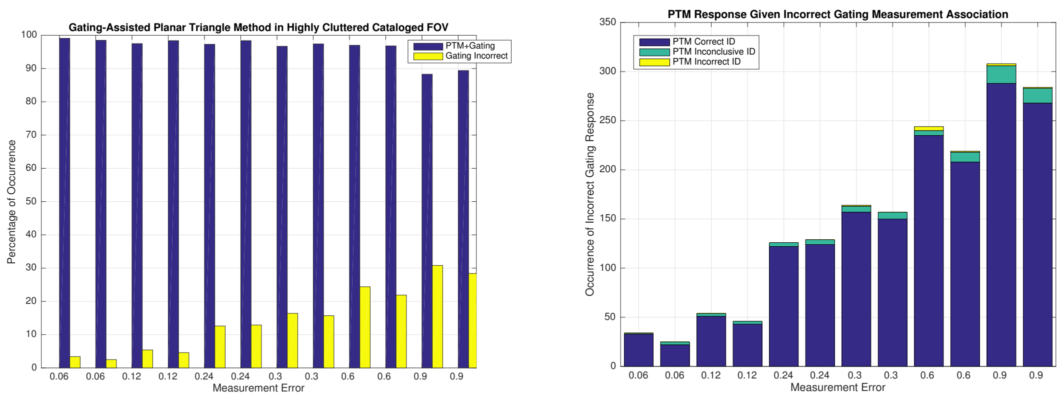

(a) **Gating-Assisted PTM and Incorrect Gating ID's**

(b) **Breakdown of PTM Response to Incorrect Gating ID's**

Figure 12. Gating-Assisted PTM Performance with Incorrect Gating ID's in Highly Cluttered FOV

(temporal) filtering-based methods. Therefore, actual stars in the FOV can be treated as false objects. Clearly by adding three times the number of false objects than the number of real objects, the simulation case is extremely challenging. The PTM approach alone would unlikely be able to provide any solution given the low probability of selecting real objects out of the FOV, and without using an extraordinarily high pivot limit. But the gating method will help match measurements to existing objects based on the Mahalanobis distance. Results show excellent performance of the gating-assisted PTM. Figures 13(a) and 13(b) demonstrate the ability of the gating-assisted PTM to overcome significant numbers of false objects and measurement uncertainty to provide the correct object association. Compared to the true object case, the false object case shows more dependency on measurement noise, but still remains comparable. Again, Figure 13(b) demonstrates the benefit of the hybrid gating-assisted PTM, where incorrect associations from gating are corrected a majority of the time via the PTM. The false object case shows more conditions where the PTM could not achieve an object association given the incorrect gating association. Although not ideal, the rejection of the gating-associated values is still a significant improvement over the gating method alone.

A paired-sample t-test is conducted to compare the mean accuracy of the PTM versus the PTM with

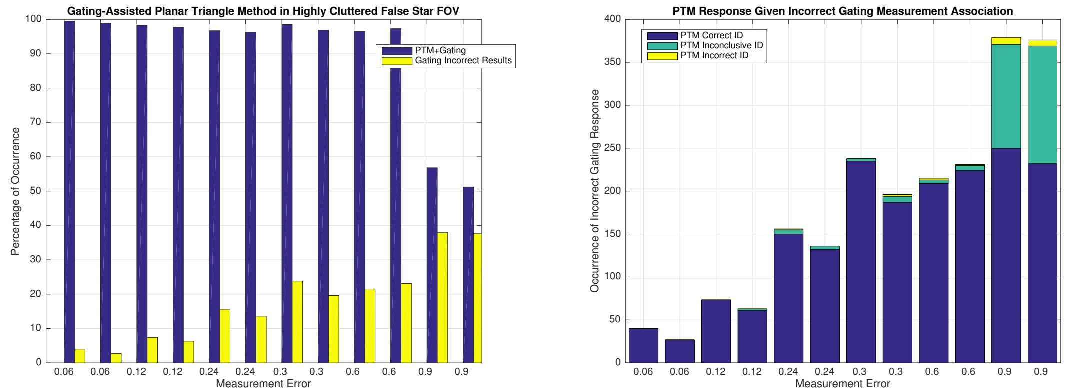

(a) **Gating-Assisted PTM and Incorrect Gating ID's with False Stars**

(b) **Breakdown of PTM Response to Incorrect Gating ID's**

Figure 13. Gating-Assisted PTM Performance with Incorrect Gating ID's in Highly Cluttered False Star FOV

gates using the IBM SPSS 19 Statistical Software. The summarized results in Tables $3-4$ show a significant difference between the accuracy of PTM with gates (Mean = 91.32, S.D. = 13.164) and PTM alone (Mean = 83.52, S.D. = 13.841) with $t = 11.415$ at $p = 0.01$. From these results it is concluded that PTM with gates is 7.801% $(\text{Mean} = 7.801, \text{S.D.} = 2.899)$ more accurate than PTM alone with a 99% confidence interval.

Table 3. Paired Samples Statistics

	Mean	N	Std. Deviation	Std. Error Mean
PTM Gate	91.32	18	13.164	3.103
PTM	83.52	18	13.841	3.262

	N	Correlation	Sig
PTM Gate & PTM	18	0.978	0.000

Table 4. Paired Samples Test for Difference Between PTM Gate and PTM Only

Paired Differences							
			99 % Confidence Interval of the Difference				
Mean	Std. Deviation	Std. Error Mean	Lower	Upper	t	df	Sig. (2-tailed)
7.801	2.899	0.683	5.820	9.782	11.415	17	0.000

VII. Conclusions

This work extends the concepts of using ellipsoidal validation gates to data association and pattern recognition algorithms such the planar triangle method (PTM). The proposed method of using a ellipsoidal gating as a precursor to the PTM shows improvement in accuracy of objects being correctly associated when compared to the PTM or gating method alone in a highly challenging field of view. This method is fairly simple and compact in implementation, but the results show a significant improvement ranging anywhere from 5% to 20% depending on the measurement errors involved. The greatest improvement in successful object association is shown in high measurement uncertainty simulations. Due to the lack of a reliable screening method, the gating method is most likely not a feasible association algorithm on its own. As uncertainty rises, the gating method yields significantly more incorrect results while the PTM often yields inconclusive associations. When the gating method is joined with the PTM, a significant improvement in robustness and accuracy is realized. The synergistic effect of combining the two methods removes certain disadvantages of each. The PTM provides additional screening and checking to the gating output data, while the gating output data provides a verified starting point for the PTM to begin its search. The addition of a smart pivoting index as an output of the gating method proves to increase reliability of the PTM.

VIII. Future Work

Investigation into an even more intelligent and streamlined interface between gating and PTM algorithms could provide savings in computation and additional increases in accuracy. Potentially, using the Mahalanobis distance to dictate the next pivot from an unlikely object to a more likely measurement, could provide additional benefits. Further exploration into data association for non-Gaussian errors could make a stronger case for implementation as orbit errors are often non-Gaussian. More advanced data association techniques can be used that do not make an assumption of the form of the uncertainty of the measurement.

References

[1]NASA, "International Space Station Performs Fourth and Fifth Debris Avoidance Maneuvers of 2014," *Orbital Debris Quaterly News*, Vol. 19, NASA, Jan. 2015, pp. 1–2.

[2]Silversmith, P. E., *Space-Object Identification Using Spatial Pattern Recognition*, Master's thesis, University at Buffalo, State University of New York, 2013.

[3]Hill, K., Alfriend, K. T., and Sabol, C., "Covariance-based Uncorrelated Track Association," *AIAA/AAS Astrodynamics Specialist Conference and Exhibit*, Honolulu, HI, 2008, AIAA 2008-7211, doi:10.2514/6.2008-7211.

[4]Giza, D., Singla, P., Crassidis, J., Linares, R., Cefola, P., and Hill, K., "Entropy-Based Space Object Data Association Using an Adaptive Gaussian Sum Filter," *AIAA/AAS Astrodynamics Specialist Conference*, Toronto, ON, Canada, 2010, AIAA 2010-7526, doi:10.2514/6.2010-7526.

[5]DeMars, K. J., Hussein, I. I., Frueh, C., Jah, M. K., and Erwin, R. S., "Multiple-Object Space Surveillance Tracking Using Finite-Set Statistics," *Journal of Guidance, Control, and Dynamics*, Vol. 38, No. 9, March 2015, pp. 1741–1756, doi:10.2514/1.G000987.

[6]Cheng, Y., DeMars, K., and Früh, C., "Gaussian Mixture PHD Filter for Space Object Tracking," *AAS/AIAA Space Flight Mechanics Meeting*, Kauai, HI, 2013, AAS 13-242.

[7]Jones, B. A. and Vo, B.-N., "A Labeled Multi-Bernoulli Filter for Space Object Tracking," *AAS/AIAA Space Flight Mechanics Meeting*, Williamsburg, VA, 2014, AAS 15-413.

[8]Holzinger, M. J., "Using Magnetometers for Space Object Characterization in Space Situational Awareness Applications," *Journal of Guidance, Control, and Dynamics*, Vol. 37, No. 5, Sept.-Oct. 2014, pp. 1397–1405, doi:10.2514/1.G000523.

[9]Spratling, B. B. and Mortari, D., "A Survey on Star Identification Algorithms," *Algorithms*, Vol. 2, No. 1, Jan. 2009, pp. 93–107, doi:10.3390/a2010093.

[10]Cole, C. L. and Crassidis, J. L., "Fast Star-Pattern Recognition Using Planar Triangles," *Journal of Guidance, Control, and Dynamics*, Vol. 29, No. 1, Jan.-Feb. 2006, pp. 64–71, doi:10.2514/1.13314.

[11]Blackman, S. and Popoli, R., *Design and Analysis of Modern Tracking Systems*, Artech House, Boston, MA, 1999.

[12]Schaub, H. and Junkins, J. L., *Analytical Mechnics of Space Systems*, American Institute of Aeronautics and Astronautics, Inc., Reston, Virginia, 2nd ed., 2009.

[13]Light, D. L., "Satellite Photogrammetry," *Manual of Photogrammetry*, edited by C. C. Slama, chap. 17, American Society of Photogrammetry, Falls Church, VA, 4th ed., 1980.

[14]Vallado, D. A., *Fundamentals of Astrodynamics and Applications*, Microcosm Press, Torrance, CA, 4th ed., 2013.

[15]Shuster, M. D., "Kalman Filtering of Spacecraft Attitude and the QUEST Model," *Journal of the Astronautical Sciences*, Vol. 38, No. 3, July-Sept. 1990, pp. 377–393.

[16]Shuster, M. D. and Oh, S. D., "Three-Axis Attitude Determination from Vector Observations," *Journal of Guidance and Control*, Vol. 4, No. 1, Jan.-Feb. 1981, pp. 70–77, doi:10.2514/3.19717.

[17]Cheng, Y., Crassidis, J. L., and Markley, F. L., "Attitude Estimation for Large Field-of-View Sensors," *Journal of the Astronautical Sciences*, Vol. 54, No. 3&4, July-Dec. 2006, pp. 433–448.

[18]Hinks, J. C. and Crassidis, J. L., "Covariance Analysis of Maximum Likelihood Attitude Estimation," *The Journal of the Astronautical Sciences*, Vol. 60, No. 2, 2013, pp. 186–210, doi:10.1007/s40295-014-0028-7.

[19]Cole, C. L., *Fast Star Pattern Recognition Using Spherical Triangles*, Master's thesis, University at Buffalo, State University of New York, 2004.

[20]Mortari, D., "A Fast On-Board Autonomous Attitude Determination System Based on a new Star-ID Technique for a Wide FOV Star Tracker," *AAS/AIAA Space Flight Mechanics Meeting*, Austin, TX, 1996, AAS 96-158.

[21]Leung, H., Hu, Z., and Blanchette, M., "Evaluation of multiple target track initiation techniques in real radar tracking environments," *IEE Proceedings - Radar, Sonar and Navigation*, Vol. 143, No. 4, Aug. 1996, pp. 246–254, doi:10.1049/ip-rsn:19960404.

[22]Johnson, N. L., Stansbery, E., Liou, J.-C., Horstman, M., Stokely, C., and Whitlock, D., "The Characteristics and Consequences of the Break-Up of the Fengyun-1C Spacecraft," *Acta Astronautica*, Vol. 63, No. 1, July-Aug. 2008, pp. 128–135, doi:10.1016/j.actaastro.2007.12.044.